Acta Materialia 178 (2019) 59-67

Monoclinic angle, shear response, and minimum energy pathways of NiTiCu martensite phases from *ab initio* calculations

Sam Bakhtiari[1], Jefferson Zhe Liu[2], Yinong Liu[1*], Hong Yang[1]

[1] Laboratory for Functional Materials, Department of Mechanical Engineering, The University of Western Australia, 35 Stirling Highway, Perth, WA 6009, Australia

[2] Department of Mechanical Engineering, The University of Melbourne, Parkville, VIC 3010, Australia

*Corresponding author email address: yinong.liu@uwa.edu.au, Phone: +61 8 6488 5664, Fax: +61 8 6488 1024.

Abstract

$Ti_{50}Ni_{50-x}Cu_x$ alloys are observed to exhibit multiple martensitic transformations from B2 to an orthorhombic B19 and a monoclinic B19′ phase. In addition, DFT calculations have predicted a B19″ phase with a higher monoclinic angle as the thermodynamically stable ground state. This study investigated the effects of Cu content and shear stress on the monoclinic angles, phase stabilities of the various martensites, the minimum energy pathways, and the relative total energies among the phases in this pseudo-equiatomic $Ti(Ni_{50-x}Cu_x)$ system. A new monoclinic phase ($B19_M$) with a monoclinic angle lower than that of B19′ was found at above a critical Cu content. This confirms the formation of an intermediate phase in the martensitic transformation sequence of the pseudo-equiatomic $Ti(Ni_{50-x}Cu_x)$ system but contradicts the crystal structure of the experimentally observed phase. It was found that the monoclinic angles of both $B19_M$ and B19″ decrease with increasing the magnitude of an opposing shear stress to their monoclinic distortion. At above certain critical values of the opposing shear stress, the $B19_M$ and B19″ phases destabilise and transform to lower monoclinic angle phases. In addition, the evidence suggests that the experimentally observed monoclinic B19′ phase is in fact a distorted B19″ with a reduced monoclinic angle under an opposing shear stress. With the same argument, the experimentally reported B19 phase is a metastable phase formed under the effect of an opposing shear stress to the monoclinic distortion of $B19_M$.

Keywords: Shape memory alloy; Martensitic phase transition; Ab initio calculations; Minimum energy pathway.

1. Introduction

NiTi shape memory alloys (SMAs) are known to exhibit unique thermomechanical properties including the shape memory effect and pseudoelasticity [1]. These properties originate from the thermoelastic martensitic transformations in these alloys [2, 3]. Owing to these remarkable properties, they have been used in many innovative designs, both in end product applications, such as low power actuators in automotive industry [4], wing morphing control in aerospace

engineering [5], miniature actuators in microelectromechanical systems (MEMS) [6], actuators in robotics [7] and biomedical devices [8], and in novel materials designs, such as intermetallic composites [9], functionally graded designs [10-13], and smart architectured materials [14]. To meet demands of different applications, their martensitic transformation characteristics and thermomechanical properties often need to be altered and controlled. One commonly used method to alter and control the properties is to add a third element into the binary NiTi, such as Cu, Nb, Hf and Pd [15-19]. Among them, Cu substitution for Ni is known to introduce an intermediate orthorhombic B19 phase in its martensitic transformation sequence, to narrow the transformation hysteresis [20], and to enhance thermal and mechanical cycling stability [21, 22]. These characteristics of ternary NiTiCu alloys make them attractive choices for many applications.

Solution treated equiatomic NiTi alloys are known to exhibit a B2 austenite and a B19′ monoclinic martensite phase. Furthermore, density functional theory (DFT) calculations have also identified two other martensitic phases to B2 at 0 K, including a monoclinic B19″ and a base-centred orthorhombic (BCO) phase [23, 24]. The BCO phase is the ground state at 0 K. Experimentally, those two phases are not observed though they are energetically stable phases in DFT calculations. In contrast, the experimentally observed B19′ monoclinic martensite is thermodynamically unstable in DFT calculations [23, 25]. Stabilisation of B19′ requires either an opposing shear stress to its monoclinic distortion [25] or a hydrostatic pressure [26, 27]. A recent DFT calculation suggests that inclusion of the thermal vibrational effect at a certain temperature may change the relative energy state order of the martensitic phases [28]. For example, a monoclinic structure with an angle of ~101°, which corresponds to B19″, is the ground state martensite instead of BCO at above 200 K.

Complex transformation routes have been suggested among these phases of equiatomic NiTi. The experimentally observed martensitic transformation from B2 to B19′ has been hypothesised to occur phenomenologically in two steps [1, 29]. The first step is B2→B19. This transformation is associated with a volumetric lattice contraction and shuffling of the Ni and Ti atoms along the $[010]_{B19}$ direction. This produces the orthorhombic structure of the B19 phase. The second step is B19→B19′. It involves a non-basal shear along $[010]_{B19}$ direction and shuffling of Ni and Ti in the direction of $[001]_{B19}$. Further shear along $[010]_{B19}$ direction to reach 101.6° and shuffle of Ni and Ti in the direction of $[001]_{B19}$ produces B19″, and then finally at ~107° monoclinic angle, BCO crystal structure forms. The B19 orthorhombic phase is imaginary for binary NiTi.

In $Ti_{50}Ni_{50-x}Cu_x$ alloys when the Cu content exceeds 7.5 at%, the original B2↔B19′ one-step transformation sequence has been observed to change to two steps, i.e., B2↔B19↔B19′ [15, 20, 30, 31]. When $x \geq 15$ at%, B19′ vanishes and the transformation sequence becomes B2↔B19 [32]. However, some recent studies have shown that the B19′ phase can still be present in alloys of 16 and 20 at% Cu contents [33, 34].

Although the B19 phase has been well observed experimentally and the empirical criterion for its formation is established, a clear theoretical ground to explain the formation of the B19 phase and the change of the transformation sequence from B2↔ B19′ to B2↔B19↔B19′ and then to B2↔B19 with increasing Cu content is lacking in the literature.

In this study, the effect of Cu content on the structures of the phases in the pseudo-equiatomic $Ti(Ni_{50-x}Cu_x)$ system was investigated by means of density functional theory (DFT) calculation. Pure shear stresses were applied to study the stability of the martensitic phases under such conditions to establish fundamental understandings of the behaviour of the real alloy system.

2. Methodology

The DFT simulations were carried out using Vienna *ab initio* Simulations Package (VASP) [35]. The PBE exchange-correlation functional [36] and the projector-augmented method (PAW) [37] were employed to perform the simulations. All calculations applied an energy cut-off of 500 eV, an electronic energy convergence criterion of 1×10^{-7} eV, and the *k*-point mesh density of at least 50 *k*-points per $Å^{-1}$. The maximum force on each atom after relaxation was less than 5×10^{-3} $eVÅ^{-1}$ and the simulations were spin polarised. The minimum energy pathways (MEP) between fully relaxed structures were performed using the generalised solid-state nudge elastic band (G-SSNEB) method implemented in the VTST package [38]. The initial transition path between two fully relaxed structures was constructed by linearly interpolating the cell vectors and ionic positions for eight intermediate images. The method is capable of changing shape, size and ionic positions of intermediate images between two fully relaxed phases to find the energetically lowest possible states.

The size of the supercells for the most of the DFT calculations for the effects of pure shear and for the minimum energy pathways was 32 atoms, created from 2×2×2 four-atom primitive unit cells. The Cu addition was achieved through random Ni atom substitution for each composition. Given the limited supercell size, only four Cu contents of x=0, 3.125, 6.250, 9.375 and 12.500 at% were investigated. For each Cu content, three different Cu doping patterns were calculated to avoid artefacts from doping patterns. In this study, the BCO phase is not considered due to the limited size of the employed supercells, which could easily break the high symmetry of the BCO phase. To validate the results of the 2×2×2 supercell calculations, especially the formation of the new phase and the monoclinic angle of the martensite phases, 3×3×3 supercells (containing 108 atoms) of special quasi-random structures (SQS) [39] were generated for different Cu contents. The SQS method mimics the correlation functions of a perfectly random structure and can approximate the random solid solution [39].

A geometry-controlled calculation was performed to determine the resistive and assistive shear stresses required to distort the monoclinic angle of a phase from tis relaxed state. The calculation was completed using the VASP automatic relaxation routine via optimisation of the lattice parameters and relaxation of ionic positions. Then the lattice parameters are optimised by reducing all stress components to 0.01 GPa except the shear stress corresponding to the monoclinic angle distortion applied. This process allows a pure shear stress corresponding to the applied monoclinic distortion to be calculated. Fig. 1 shows the changes of the total energy and the lattice parameters of B19′ in $Ti_{50}Ni_{37.5}Cu_{12.5}$ when the monoclinic angle is set at 95º, which is a -3º distortion from the 98º at its relaxed state. The iterations were continued until the total energy convergence criterion of 10^{-7} eV/atom is reached and the maximum force on each atom is below 5×10^{-3} $eVÅ^{-1}$.

Using this approach, the shear stress thus calculated is a function of the monoclinic angle distortion from its relaxed state. The maximum shear stress (positive or negative) on monoclinic distortion (increase or decrease) of a monoclinic phase signifies the critical condition at which the phase becomes energetically unfavourable and beyond which the phase transforms to a new phase with a higher or lower monoclinic angle. These maximum stresses are thus the critical shear stresses for transformations.

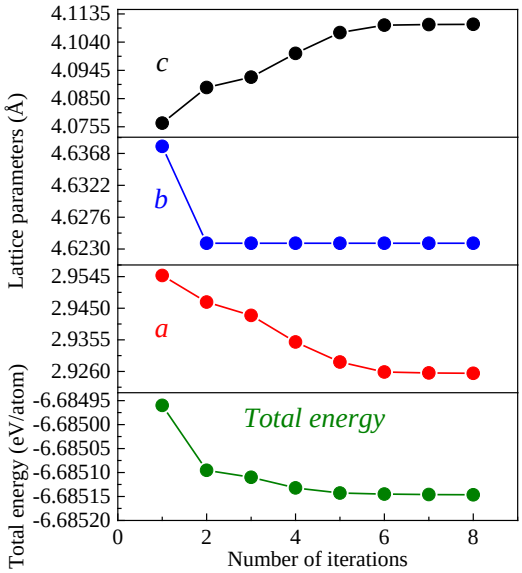

Figure 1. Optimisation of the total energy and the lattice parameters of B19″ in $Ti_{50}Ni_{37.5}Cu_{12.5}$ at 95° monoclinic angle, which is a -3° distortion from its relaxed state.

3. Results and discussions

Fig. 2 shows the effect of Cu addition on the monoclinic angles of the martensitic phases in the Ti(Ni, Cu) pseudo-equiatomic system. It is seen that the monoclinic angle of B19″ decreases with increasing Cu content. The monoclinic angle difference between the 2×2×2 (circular blue data points) and 3×3×3 (rectangular blue data points) supercells is negligible. The B19′ phase is not a thermodynamically stable phase, thus it cannot be predicted by DFT calculation. The data shown in the figure are experimental data reported in the literature [30, 40]. It is seen that the monoclinic angle of B19′ also decreases with increasing Cu content. There is a clear difference between the monoclinic angles of B19″ (calculated) and B19′ (experimental) phases.

Our DFT calculations also revealed another monoclinic phase at above a critical Cu content, denoted $B19_M$ in Fig. 2. To form the $B19_M$ phase, a large enough (i.e. 1°) increase or decrease of monoclinic distortion can be applied to the relaxed B19 or B19″ phases, respectively. Subsequent VASP automatic relaxation may stabilise the $B19_M$ phase. A small distortion reverts back to the fully relaxed distorted structure. Apparently, at below the critical Cu content, the distorted B19″ transforms to B19 and vice versa. The critical Cu content for the stabilisation of the $B19_M$ phase for 2×2×2 and 3×3×3 supercells are x = 6.25 at % and 9.25 at%, respectively. The difference in the critical Cu content to stabilise the new phase can be attributed to the limitations of the smaller supercells, and the value obtained from the larger supercells is expected to better approximate the random solid solution condition. To further investigate the onset of the stabilisation of the $B19_M$ phase, a 4×4×4 (256 atoms) SQS supercell with x = 9.375 at% was constructed. The increase of the size of the supercell did not affect the monoclinic angle or the onset of the stabilisation.

The presence of this new phase at above 9.25 at% Cu in the DFT calculation coincides with the presence of the B19 phase at above 7.5 at% Cu in experiment [15]. However, the monoclinic crystal structure of the $B19_M$ phase predicted by the calculation contradicts the experimentally observed orthorhombic phase (B19). The monoclinic angle of this phase is below those of B19′ (experimental) and B19″ (calculated) phases. This phase is denoted $B19_M$ in recognition of its monoclinic lattice distortion. Its monoclinic angle is also calculated and

found to decrease with increasing Cu content. Fig. 2 also presents the calculated B19 phase at different Cu contents. The data points shown in the figure for the B19 phase are the fully relaxed phases. No change to its orthorhombic angle is expected with changing the Cu content.

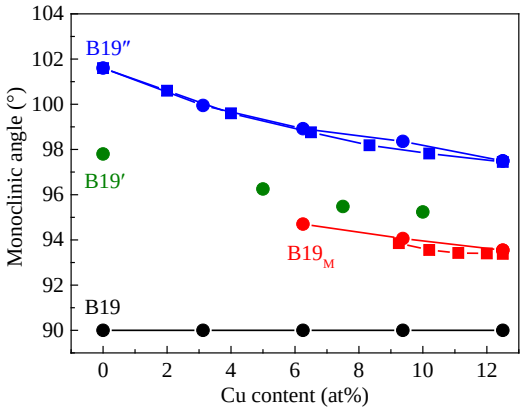

Figure 2. Effect of Cu content on the monoclinic angles of martensites in the pseudo-equiatomic Ti(Ni50-xCux) system. The data for B19′ are from experimental measurements [30, 40]. (The circular and rectangular data points are calculated from 2×2×2 and 3×3×3 supercells, respectively).

In DFT calculations, the B19′ phase is known to be thermodynamically unstable, i.e., it does not exist except under the influences of external factors such as a resistive shear stress [25] (a shear stress opposing the monoclinic distortion of the phase) or a hydrostatic pressure [26, 27]. The resistive shear stress and hydrostatic pressure can be self-generated during the martensitic phase transformation because B2→B19″ (and also B2→B19′) is associated with a monoclinic lattice distortion and a volume expansion. In our previous work [27], we revealed that the B19′ structure can be stabilised at 2 GPa hydrostatic pressure without the presence of a resistive shear stress. Increase of the hydrostatic pressure reduces the monoclinic angle of the martensite phases and induces the B19″→B19′ transformation at ~6.3 GPa and the BCO→B19′ transformation at ~9 GPa [27].

The B19′ structure can also be achieved by applying a resistive shear stress to B19″. Fig. 3 shows the effect of a resistive shear stress on the monoclinic angle, relative total energy, and phase stability of B19″ in the $Ti_{50}Ni_{50}$ alloy system (i.e., x = 0 at% Cu). Fig. 3(a) shows the effect of resistive shear stress on the monoclinic angle and phase stability of B19″. The calculation shows that the monoclinic angle of B19″ decreases progressively with increasing the magnitude of the resistive shear stress and that at -0.85 GPa shear stress the monoclinic angle is reduced to 97.8°, the value measured experimentally for B19′. This suggests that the B19′ phase may in fact be a distorted B19″ at -0.85 GPa opposing shear stress. Further increase of the opposing shear stress destabilises B19″ towards the orthorhombic B19 (the dash line in the figure). The critical point of the destabilisation is at 95.5° monoclinic angle and -1.17 GPa shear stress. The critical monoclinic angle and resistive shear stress are in a good agreement with the previous calculation by Wagner and Windl [25]. The only difference between this work and their analysis is the initial crystal structure. In this work we applied the opposing shear stress to B19″, and they started from the BCO structure. Fig. 3(b) shows the effect of monoclinic angle, which is influenced by the resistive shear stress, on the relative total energy of B19″. The total energy of B19 relative to that of B19″ is also shown in the figure. The relative total energy of B19″ increases with decreasing the monoclinic angle (caused by the increase of the resistive shear stress) to 95.5°, at which point it destabilises into B19. The B19 phase is at a higher relative total energy position than B19″. The monoclinic angle of the

experimentally observed B19′ phase is also indicated in the figure. It is apparent that the B19′ phase is not a local minimum under shear stress.

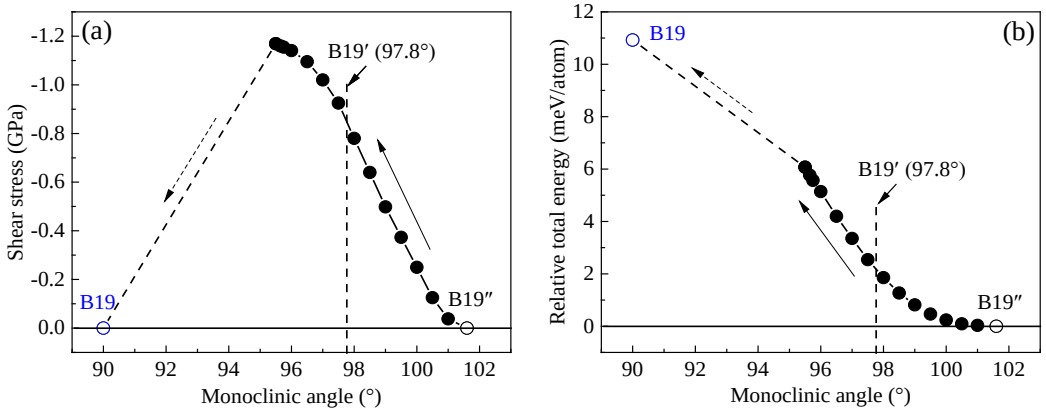

Figure 3. $Ti_{50}Ni_{50}$ alloy system. (a) effect of resistive shear stress on the monoclinic angle and phase stability of B19″; (b) effect of resistive shear stress on the relative total energy of B19″ as reflected by the variation of the monoclinic angle.

Similar to the equiatomic NiTi case, shear stresses can be applied to the martensitic phases of the pseudo-equiatomic $Ti(Ni_{50-x}Cu_x)$ system to achieve the experimentally reported B19′ and also to reveal the shear response of $B19_M$. Fig. 4 shows the effect of a resistive shear stress on $B19_M$ and B19″ in the $Ti_{50}Ni_{43.75}Cu_{6.25}$ alloy system. Fig. 4(a) shows the effect of the shear stress on the monoclinic angles and phase stabilities of the two phases. The monoclinic angle of B19″ decreases with increasing the opposing shear stress. At -0.75 GPa shear stress, the monoclinic angle is reduced to 95.5° and B19″ destabilises towards $B19_M$. Comparing with the case for equiatomic NiTi, the Cu substitution for Ni decreases the critical shear stress required to destabilise B19″. A linear interpolation between the experimentally reported monoclinic angles of B19′ (see Fig. 2) at 5 and 7.5 at% Cu reveals a monoclinic angle of 95.9° for B19′ at 6.25 at% Cu, which is indicated in the figure. It is very close to the calculated critical destabilisation monoclinic angle of B19″ under the influence of the opposing shear stress.

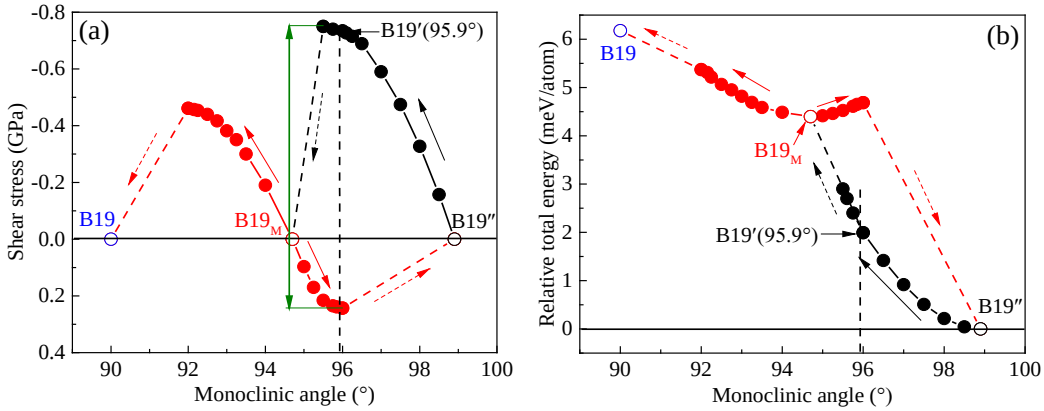

Figure 4. $Ti_{50}Ni_{43.5}Cu_{6.25}$ alloy system. (a) effect of shear stress on the monoclinic angle and phase stability of $B19_M$ and B19″; (b) effect of shear stress on the relative total energy of $B19_M$ and B19″ as reflected by the variation of the monoclinic angle.

The opposing shear stress is also applied to the $B19_M$ phase, as seen in Fig. 4(a). Similar to B19″, the monoclinic angle of $B19_M$ decreases progressively with increasing the opposing shear stress. It destabilises into B19 at the critical monoclinic angle of 92° at -0.46 GPa shear

stress. For comparison, an assistive shear stress, which is in the direction of the monoclinic distortion, is also applied to the $B19_M$ phase. In contrary with the opposing shear stress, the monoclinic angle of $B19_M$ increases progressively with increasing the assistive shear stress. At +0.24 GPa shear stress, the monoclinic angle is increased to 96° and the $B19_M$ phase is destabilised to B19″. The shear stress hysteresis for the $B19_M \leftrightarrow$B19″ transformation is 0.99 GPa as indicated by the double headed arrow in Fig. 4(a).

Fig. 4(b) shows the effect of shear stress, as reflected by the monoclinic angle change, on the relative total energies of B19″ and $B19_M$ phases. It is seen that the relative total energy of B19″ decreases with decreasing the monoclinic angle (i.e., increasing the resistive shear stress), till the critical point at 95.5° when B19″ becomes unstable and transforms to $B19_M$, as indicated by the dashed line. In comparison, the relative total energy of $B19_M$ increases with both increasing and decreasing the monoclinic angle (corresponding to the increase of both an assistive and a resistive shear stress, respectively). This means that $B19_M$ is a local shear minimum. The $B19_M$ phase becomes unstable when the monoclinic angle is reduced to 92° and transforms to B19 under the influence of a resistive shear stress, or when the monoclinic angle is increased to 96° and transforms to B19″ under the influence of an assisting shear stress. The shear energy barrier of $B19_M \rightarrow$B19″ phase transformation is ~0.3 meV/atom. The total energy of B19 relative to that of B19″ is also shown in the figure. It is seen that the relative total energy of B19 is above those of both $B19_M$ and B19″. Also in comparison with the relative total energy of B19 in the equiatomic NiTi alloy, the addition of Cu has lowered the total energy of B19 relative to that of B19″.

Similar calculations have also been performed for x=12.5 at%. Fig. 5 shows the effects of shear stress on the $B19_M$ and B19″ phases in the $Ti_{50}Ni_{37.5}Cu_{12.5}$ alloy. Fig. 5(a) shows the effects of shear stress on the monoclinic angles and phase stabilities of $B19_M$ and B19″. Similar to the previous two cases, the monoclinic angle of B19″ decreases with increasing the opposing shear stress. At -0.72 GPa shear stress the monoclinic angle is reduced to 95° and B19″ becomes unstable and transforms to $B19_M$. The values of the shear stress and monoclinic angle of the critical point for B19″$\rightarrow B19_M$ are both slightly lower than those for the $Ti_{50}Ni_{43.5}Cu_{6.25}$ alloy. The monoclinic angle of B19′ corresponding to this alloy composition was estimated via linear extrapolation from the experimental data shown in Fig. 2 to be 95.1°, as indicate in the figure. It is very close to the calculated critical monoclinic angle of B19″ under the influence of an opposing shear stress.

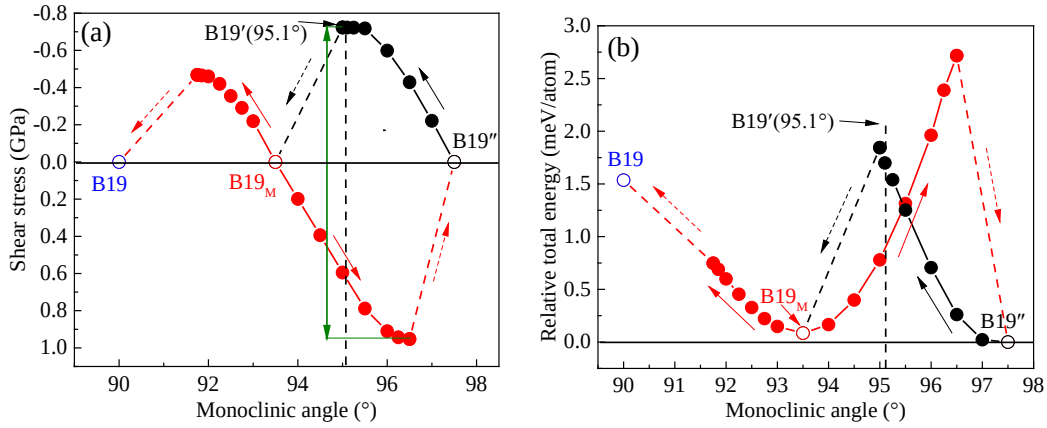

Figure 5. $Ti_{50}Ni_{37.5}Cu_{12.5}$ alloy system. (a) effect of shear stress on the monoclinic angle and phase stability of $B19_M$ and B19″; (b) effect of shear stress on the relative total energy of $B19_M$ and B19″ as reflected by the variation of the monoclinic angle.

The opposing shear stress is also applied to $B19_M$ phase. Similar to B19″, the monoclinic angle of $B19_M$ decreases progressively with increasing the opposing shear stress. The critical monoclinic angle is 91.75° and the critical shear stress is -0.45 GPa for the $B19_M \rightarrow B19$ transformation. When an assistive shear stress is applied to $B19_M$, the monoclinic angle increases progressively till 96.5° at +0.95 GPa shear stress when it becomes unstable and transforms to B19″. The shear stress hysteresis for the $B19_M \leftrightarrow B19''$ transformation is 1.67 GPa, which is much higher than that for the $Ti_{50}Ni_{43.5}Cu_{6.25}$ alloy.

Fig. 5(b) shows the effect of shear stress, as reflected by the variation of the monoclinic angle, on the relative total energies of the martensite phases. The relative total energy of B19″ decreases with decreasing the monoclinic angle (increasing the opposing shear stress). There is a shear energy barrier of 1.84 meV/atom for $B19'' \rightarrow B19_M$. $B19_M$ is still a local shear minimum. The reverse $B19_M \rightarrow B19''$ transformation may occur by the application of an assisting shear stress (a shear stress in the direction of the monoclinic distortion, thus increase of the monoclinic angle). The shear energy barrier of the $B19_M \rightarrow B19''$ transformation is ~2.72 meV/atom, which is higher than that for the $Ti_{50}Ni_{43.5}Cu_{6.25}$ alloy. This implies that $B19_M$ is further stabilised relative to B19″ at higher Cu contents.

Values of the shear stresses and the monoclinic angles at the critical points for the $B19_M \rightarrow B19$, $B19_M \rightarrow B19''$, and $B19'' \rightarrow B19_M$ phase transformations as determined from the above calculations are summarised in Table 1. Also derived from these values are the shear stress hysteresis ($\Delta\tau$) for $B19'' \leftrightarrow B19_M$. It is seen that by increasing the Cu content in the pseudo-equiatomic $Ti(Ni_{50-x}Cu_x)$ system, the critical resistive shear stress required to destabilise B19″ phase reduces. It can also be seen that the critical resistive shear value to destabilise B19″ is higher than that of $B19_M$. The increase of the Cu content also increases the shear hysteresis of the $B19_M \leftrightarrow B19''$ transformation. The increase of the shear hysteresis can be interpreted as stabilisation of $B19_M$ relative to B19″.

Table 1. Summary of the calculated shear stresses, monoclinic angles, and shear hysteresis at the critical points for the $B19_M \rightarrow B19$, $B19_M \rightarrow B19''$, and $B19'' \rightarrow B19_M$ phase transformations.

at% Cu	$B19_M \rightarrow B19$		$B19_M \rightarrow B19''$		$B19'' \rightarrow B19_M(B19)$		$B19'' \leftrightarrow B19_M$
	τ(GPa)	β(°)	τ(GPa)	β(°)	τ(GPa)	β(°)	Δτ(GPa)
0	-	-	-	-	-1.17	95.5	-
6.25	-0.46	92	+0.24	96	-0.75	95.5	+0.99
12.5	-0.45	91.75	+0.95	96.5	-0.72	95	+1.67

According to these findings, the theoretical thermal transformation sequence is expected to be $B2 \leftrightarrow B19''$ (BCO phase is not considered in this discussion) at Cu < 9.25 at% and is $B2 \leftrightarrow B19_M \leftrightarrow B19''$ at Cu ≥ 9.25 at%, when under no external influences (e.g., shear stress or hydrostatic pressure). The DFT prediction of the appearance of the intermediate $B19_M$ phase at above 9.25 at% Cu coincides with the experimental observation of the B19 phase [15, 20, 30, 31]. However, there exist a couple of discrepancies between the theoretical calculations and experimental observations. First, at below 9.25 at% Cu, the predicted martensite is B19″ whereas the experimentally observed martensite is B19′, which has a smaller monoclinic angle. Secondly, Cu ≥ 9.25 at%, the experimentally observed intermediate phase is B19, which has an orthorhombic structure, whereas the theoretically predicted phase is $B19_M$, which has a monoclinic structure.

The discrepancy between B19″ and B19′ has been rationalised here by the effect of the inherent resistive shear stress self-generated by the monoclinic distortion of the transformation itself. The evidence presented in Fig. 3(a) (similarly in Figs. 4(a) and 5(a)) also suggests that the B19′ phase is a distorted B19″ with a reduced monoclinic angle instead of a stable phase in its own right, since that it is not a local shear minimum but a passing state on the continuous curve of the monoclinic angle vs shear stress. This hypothesis also implicitly implies that the monoclinic angle of the experimentally observed B19′ can vary depending on the magnitude of the local opposing shear stress. Considering the stiffness tensor of B19′ martensite (taken also as for B19″) calculated by Wagner and Windl [25] and its monoclinic shear distortion, the opposing shear stress generated within a rigid body can be estimated to be ~3 GPa, apparently sufficient to reduce the monoclinic angle of B19″ to that of the experimentally observed B19′.

By the same argument, the theoretically predicted monoclinic $B19_M$ is also expected to self-generate an opposing shear stress, which will also reduce its monoclinic distortion, as expressed in Figs. 4(a) and 5(a). The self-generated resistive shear stress may well be above the critical value required to destabilise $B19_M$. This may lead to the experimentally observed orthorhombic B19 phase. This is also plausible in that the critical shear stress of $B19_M \rightarrow B19$ is significantly lower than that required for B19″→B19′.

Summarising the above analyses, it is believed that the experimentally observed B19′ is in fact a distorted B19″ with a reduced monoclinic angle and that the experimentally observed B19 is induced from $B19_M$, with both process caused by the self-generated opposing shear stress associated with the monoclinic distortion of the martensites.

To study the stabilities of the B19, $B19_M$ and B19″ phases and the possible transformation routes, the minimum energy pathways (MEPs) between them are established. Fig. 6 shows the MEPs for $B19 \leftrightarrow B19_M$ and $B19_M \leftrightarrow$B19″ phase transformations. Fig. 6(a) shows the $B19 \leftrightarrow B19_M$ transformation at three different Cu contents. The $B19_M$ phase has a lower energy state than the B19 phase, and the $B19 \rightarrow B19_M$ transformation is barrier-less, implying a spontaneous transformation and the instability of B19 (B19 is not a local minimum) under no external influences (e.g., shear stress and hydrostatic pressure). Fig. 6(b) shows the $B19_M \leftrightarrow$B19″ transformation at three different Cu contents. An energy barrier exists between the two phases for all the three cases, and its magnitude increases with increasing the Cu content. It is apparent that below the critical level of Cu content, the $B19_M \rightarrow$B19″ is barrier-less, thus the $B19_M$ structure transforms to B19″ (the ground state). The energy barrier implies that $B19_M$ can be a local minimum, which can be the reason for the formation of $B19_M$. It is also seen that the energy level of $B19_M$ is above that of B19″ but the difference between them decreases with increasing the Cu content. At 12.5 at% Cu, the two phases have similar energy levels. Following the same trend, it may be expected that at x > 12.5 at% Cu the energy level of $B19_M$ becomes lower than that of B19″, i.e. $B19_M$ becomes the ground state. This can be the reason of the reported disappearance of B19′ (B19″) from the thermal transformation sequence of B2↔B19↔B19′ [15].

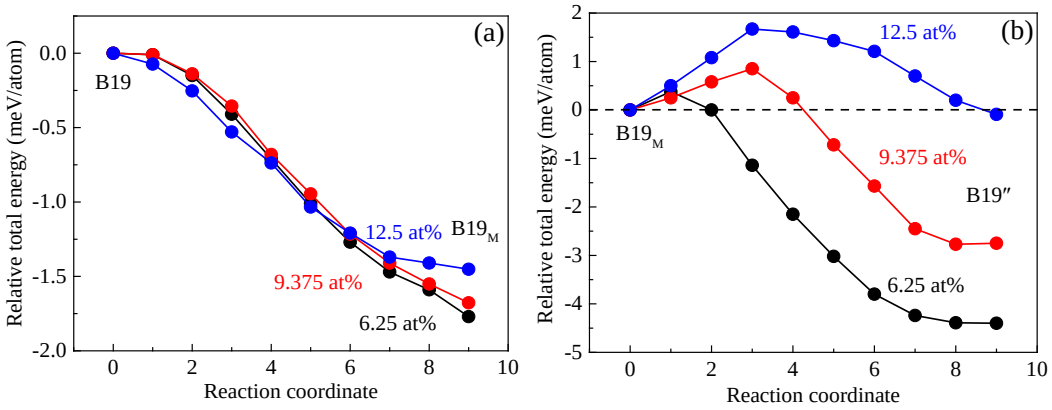

Figure 6. Minimum energy pathways between (a) B19↔B19$_M$ and (b) B19$_M$↔B19″ for the Ti(Ni$_{50-x}$Cu$_x$) system.

To further assess the stabilities of B19 and B19$_M$ phases, phonon dispersions were calculated from the frozen phonon approach using displacements of 0.01 Å in the Phonopy package [41]. Negative frequencies in a phonon dispersion implies dynamic instability of the studied crystal structure. Fig.7 shows the phonon spectra of the phases. Fig.7 (a) shows the phonon dispersion of B19 at 0 at% Cu content (i.e. equiatomic NiTi alloy system). It is seen that negative phonon frequencies are present near Γ. This reveals the instability of B19 in the equiatomic NiTi alloy system. Fig. 7(b) shows the phonon dispersion of the B19 phase at the 9.375 at% Cu content. It is seen that negative frequencies are present which implies that the Cu addition does not stabilise the B19 phase at 0 K. Fig. 7(c) shows the phonon dispersion of the newly discovered B19$_M$ at 9.375 at% Cu content. The positive frequencies reveal the stability of the phase at the studied condition.

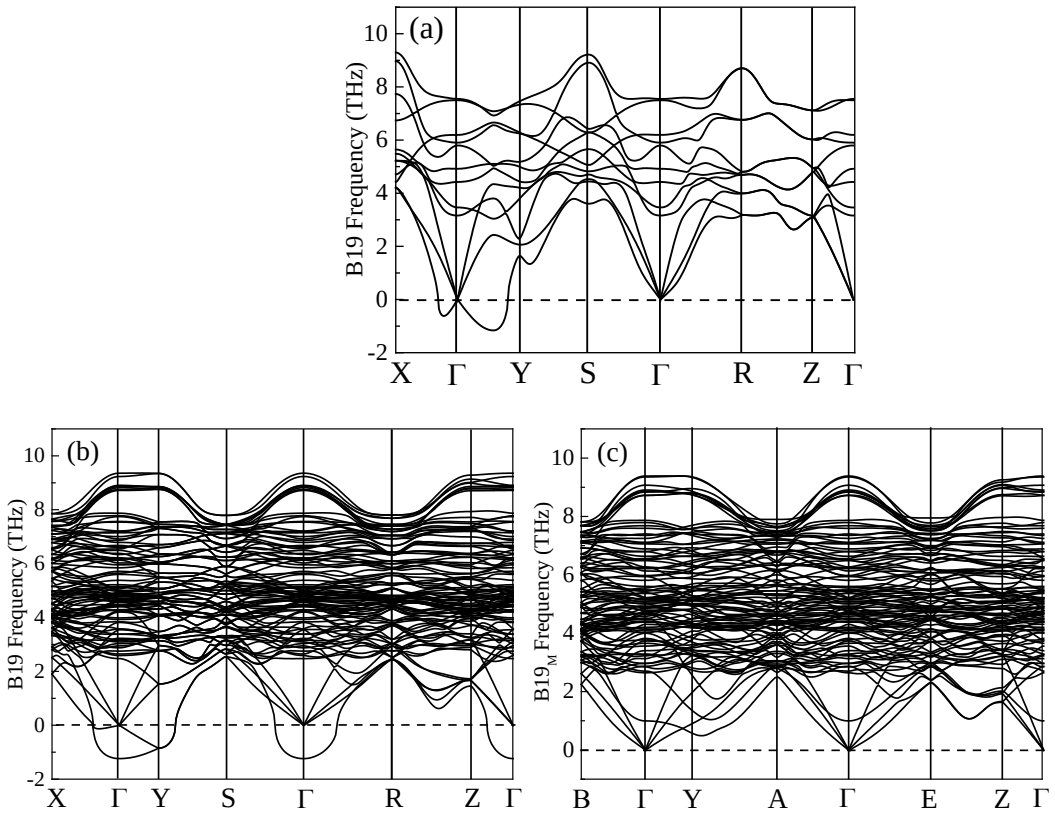

Figure 7. Phonon dispersions of (a) B19 at 0 at% Cu, (b) B19 at 9.375 at% Cu and (c) $B19_M$ at 9.375 at% Cu phases at 0 K. Phonons are extracted from simulations using 384-atom super-cells (2×2×3 super-cell of 2×2×2 four-atom primitive unit cells).

Fig. 8 shows the effect of Cu substitution for Ni on the unit cell parameters of the possible phases of pseudo-equiatomic Ti($Ni_{50-x}Cu_x$) alloy system. Fig. 8(a) shows the effect on the unit cell volume of the phases. The unit cell volumes of all the phases increase with increasing Cu content. The unit cell lattice parameters of B19′ at 0 at% Cu are experimental values adopted from Kudoh et al. [40], and at 5, 7.5, and 10 at% Cu are adopted from Nam et al. [30]. The unit cell volume of $B19_M$ is close to that of the B19 orthorhombic phase but differs clearly from that of the B19′ phase. This indicates that the experimentally observed B19′ phase is not a mistaking of the calculated $B19_M$ phase. Fig. 8(b) shows the dependences of the calculated lattice parameters of B19 and $B19_M$ on Cu content. Lattice constants *a* and *b* increase and *c* decreases with increasing Cu content for both phases. Apparently, at 12.5at% Cu, the unit-cell volume and the lattice parameters *a* and *c* of B19 and $B19_M$ become very close, but *b* and the monoclinic angels (Fig. 2) remain still different. Fig. 8(c) shows the effect of Cu content on the lattice parameters of B19″ and B19′. The data for B19″ are calculated and the data for B19′ are experimentally measured. Lattice constants *a* increases and *b* decreases with increasing Cu substitution for Ni for both phases. Lattice constant *c* increases for B19″, but shows no clear trend for B19′ with increasing Cu content.

Comparing the different martensitic phases, B19 and $B19_M$ exhibit some partial structural similarities (i.e., similar values of unit cell volume and lattice constants *a* and *c*) whereas $B19_M$ and B19″ differ from each other in every aspect including the unit cell volume, lattice constants *a* and *c* and monoclinic angle. The higher degree of structural similarity between B19 and $B19_M$ than between $B19_M$ and B19″ explains the lower critical resistive shear stress required for the $B19_M$→B19 transformation than that for the B19″→$B19_M$ transformation (Figs. 4(a) and (5(a)).

Fig. 8(d) shows the calculated and experimentally measured lattice parameter of B2 phase with increasing Cu content. The lattice parameter for both cases increases with increasing the Cu content. The experimentally measured values are higher than those estimated by DFT calculation at all Cu contents, and the difference between the two increases with increasing the Cu content. This shows a good agreement between the calculated and measured lattice parameters.

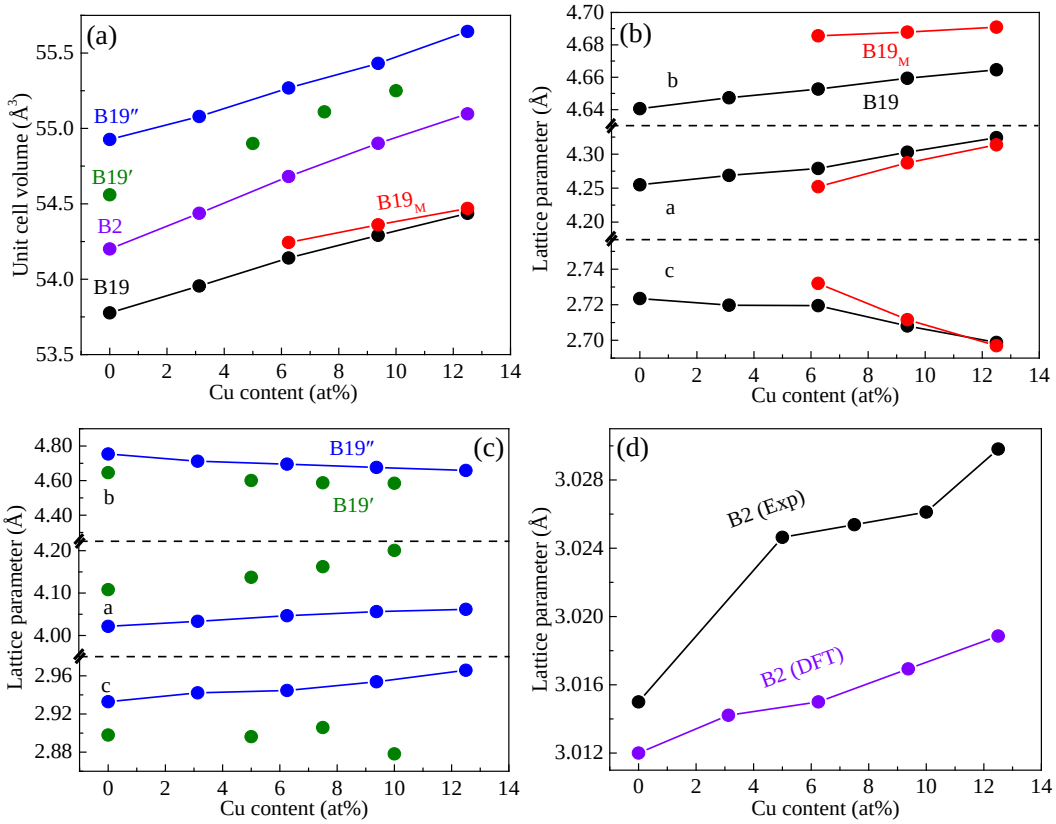

Figure 8. Effect of Cu content on the unit cell parameters of the parent and the martensitic phases of Ti(Ni$_{50-x}$Cu$_x$). (a) effect on unit cell volume; (b) effect on lattice constants of B19 and B19$_M$; (c) effect on lattice constants of B19′ and B19″; (d) effect on the lattice parameter of B2. The data for B19′ are from experimental measurements [30, 40].

Fig. 9 shows the effect of Cu content on the relative total energies of the martensitic phases of Ti$_{50}$Ni$_{50-x}$Cu$_x$ alloy, as computed by means of DFT calculations. The data are relative to the total energy of the B2 phase (the energy difference between the B2 phase and the others). The relative total energy of B19′ is computed by using the experimentally reported lattice parameters and monoclinic angle of each composition followed by a relaxation of the ionic positions. It is seen that the relative total energy of B19″ (and of B19′) increases (decrease in absolute value) with increasing Cu content. This is consistent with the experimental observation that the latent heat of the B2↔B19′ martensitic phase transformation decreases with increasing the Cu content as measured by differential scanning calorimetry (DSC) [31]. B19″ is the ground state at below 12.5 at% Cu content. For the B19 phase, relative total energy increases moderately with increasing Cu content up to 6.25 at% Cu and remains practically constant at above 6.25 at% Cu. The relative total energy of B19$_M$ is below that of B19 but above that of B19″. It is also apparent that the relative total energy levels of all martensitic phases converge and become comparable with increasing Cu content to above 12 at%. From the trend, it is expected that at above 12.5 at%, B19$_M$ becomes the ground state among the martensitic phases. Consequently, the theoretical transformation sequence becomes B2↔B19$_M$. This is consistent with the experimental observation of the one-step B2↔B19 phase transformation at above 15 at% Cu content [32].

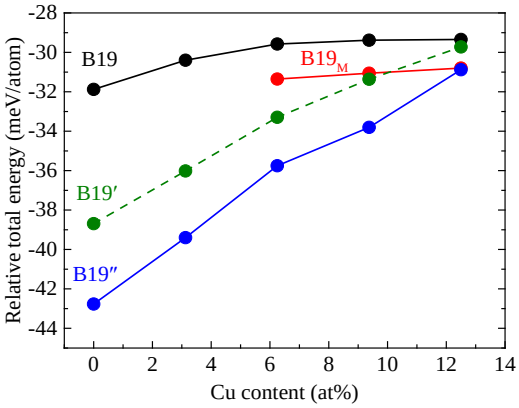

Figure 9. Effect of Cu content on the total energies of the martensitic phases relative to that of the B2 parent phase in $Ti_{50}Ni_{50-x}Cu_x$ alloy. The data for B19′ are DFT calculated using the experimentally measured unit cell parameters [30, 40].

4. Conclusions

This study investigated the effect of Cu substitution for Ni in pseudo-equiatomic $Ti(Ni_{50-x}Cu_x)$ alloy on the structures and stabilities of the various martensitic phases. The main findings are summarised below:

(1) A new monoclinic phase ($B19_M$) is identified to form at $x \geq 9.25$ at%. This phase is distinctively different from the known orthorhombic B19 and monoclinic B19′ phases.

(2) The monoclinic angles of the $B19_M$, B19′, and B19″ structures decrease with increasing the Cu content in the pseudo-equiatomic $Ti(Ni_{50-x}Cu_x)$ system.

(3) The B19→$B19_M$ transformation has a barrier-less minimum energy pathway, i.e., the B19 phase is unstable under no external influences (e.g., shear stress) and the transformation is spontaneous.

(4) The $B19_M$→B19″ transformation is associated with an energy barrier in the minimum energy pathway and the magnitude of the barrier increases with increasing the Cu content. The presence of the energy barrier indicates that $B19_M$ is a stable phase.

(5) In the pseudo-equiatomic $Ti(Ni_{50-x}Cu_x)$ system, at $x \leq 12.5$ at% B19″ is the ground state and the theoretical transformation pathway is B2↔$B19_M$↔B19″. At $x > 12.5$ at%, it is predicted that the $B19_M$ becomes the ground state and the theoretical transformation pathway changes to B2↔$B19_M$.

The evidence collected in this study also enables the following hypotheses:

(6) The experimentally observed B19′ typically with a monoclinic angle of 97.8° in binary NiTi (i.e., at x=0 at% Cu) is in fact a distorted B19″ phase with a reduced monoclinic angle from 101.6°. This can be rationalised by the inherent opposing shear stress associated with the monoclinic lattice distortion of the B19″ (and B19′) phase. In this regard, it is in essence not a thermodynamically stable phase and its monoclinic angle is expected to change depending on the actual magnitude of the opposing shear stress upon each variant.

(7) By the same argument, the experimentally observed orthorhombic B19 phase reported in the literature for Ti(Ni,Cu) alloys is in fact a metastable phase formed from $B19_M$ under the influence of an opposing shear stress. This can also be rationalised by the inherent opposing shear stress associated with the monoclinic lattice distortion of the $B19_M$ phase.

Acknowledgement

We wish to acknowledge the financial support to this work from the Australian Research Council in grant 180101955. This work was supported by resources provided by the Pawsey Supercomputing Centre with funding from the Australian Government and the Government of Western Australia, and by National Computational Infrastructure.

References

[1] K. Otsuka, X. Ren, Physical metallurgy of Ti–Ni-based shape memory alloys, Progress in materials science 50(5) (2005) 511-678.

[2] Q. Meng, Z. Wu, R. Bakhtiari, B.S. Shariat, H. Yang, Y. Liu, T.-h. Nam, A unique “fishtail-like” four-way shape memory effect of compositionally graded NiTi, Scripta Materialia 127 (2017) 84-87.

[3] Q. Meng, Z. Wu, R. Bakhtiari, J. Zhang, H. Yang, Y. Liu, Stress serration and arch-shaped Lüders stress plateau behaviour of Ti–50.8 at% Ni wire prepared by selective electrical resistance over-aging, Smart Materials and Structures 25(11) (2016) 115035.

[4] F. Butera, A. Coda, G. Vergani, S.G. SpA, Shape memory actuators for automotive applications, Nanotec IT newsletter. Roma: AIRI/nanotec IT (2007) 12-6.

[5] C. Bil, K. Massey, E.J. Abdullah, Wing morphing control with shape memory alloy actuators, Journal of Intelligent Material Systems and Structures 24(7) (2013) 879-898.

[6] M. Kohl, Shape memory microactuators, Springer Science & Business Media2013.

[7] J. Ruiz-del-Solar, E. Chown, P.G. Plöger, RoboCup 2010: Robot Soccer World Cup XIV, Springer Science & Business Media2011.

[8] L. Petrini, F. Migliavacca, Biomedical applications of shape memory alloys, Journal of Metallurgy 2011 (2011).

[9] S. Hao, L. Cui, D. Jiang, X. Han, Y. Ren, J. Jiang, Y. Liu, Z. Liu, S. Mao, Y. Wang, A transforming metal nanocomposite with large elastic strain, low modulus, and high strength, Science 339(6124) (2013) 1191-1194.

[10] B.S. Shariat, Q. Meng, A.S. Mahmud, Z. Wu, R. Bakhtiari, J. Zhang, F. Motazedian, H. Yang, G. Rio, T.-h. Nam, Experiments on deformation behaviour of functionally graded NiTi structures, Data in Brief 13 (2017) 562-568.

[11] R. Bakhtiari, B.S. Shariat, F. Motazedian, Z. Wu, J. Zhang, H. Yang, Y. Liu, Complex transformation field created by geometrical gradient design of NiTi shape memory alloy, Functional Materials Letters 10(01) (2017) 1740011.

[12] B.S. Shariat, Q. Meng, A.S. Mahmud, Z. Wu, R. Bakhtiari, J. Zhang, F. Motazedian, H. Yang, G. Rio, T.-h. Nam, Functionally graded shape memory alloys: Design, fabrication and experimental evaluation, Materials & Design 124 (2017) 225-237.

[13] B.S. Shariat, R. Bakhtiari, Y. Liu, Nonuniform transformation behaviour of NiTi in a discrete geometrical gradient design, Journal of Alloys and Compounds 774 (2018) 1260-1266.

[14] Y. Furuya, Design and material evaluation of shape memory composites, Journal of intelligent material systems and structures 7(3) (1996) 321-330.

[15] T.H. Nam, T. Saburi, K.i. Shimizu, Cu-content dependence of shape memory characteristics in Ti–Ni–Cu alloys, Materials Transactions, JIM 31(11) (1990) 959-967.

[16] H. Shi, J. Frenzel, G. Martinez, S. Van Rompaey, A. Bakulin, S. Kulkova, S. Van Aert, D. Schryvers, Site occupation of Nb atoms in ternary Ni–Ti–Nb shape memory alloys, Acta Materialia 74 (2014) 85-95.

[17] J. Frenzel, A. Wieczorek, I. Opahle, B. Maaß, R. Drautz, G. Eggeler, On the effect of alloy composition on martensite start temperatures and latent heats in Ni–Ti-based shape memory alloys, Acta Materialia 90 (2015) 213-231.

[18] S. Saghaian, H. Karaca, M. Souri, A. Turabi, R. Noebe, Tensile shape memory behavior of Ni 50.3 Ti 29.7 Hf 20 high temperature shape memory alloys, Materials & Design 101 (2016) 340-345.

[19] A.C. Coppa, M. Kapoor, R. Noebe, G.B. Thompson, The compositional stability of the P-phase in Ni–Ti–Pd shape memory alloys, Intermetallics 67 (2015) 56-62.

[20] L. Gou, Y. Liu, T.Y. Ng, An investigation on the crystal structures of Ti 50 Ni 50− x Cu x shape memory alloys based on density functional theory calculations, Intermetallics 53 (2014) 20-25.

[21] D. Dye, Shape memory alloys: Towards practical actuators, Nature materials 14(8) (2015) 760-761.

[22] C. Chluba, W. Ge, R.L. de Miranda, J. Strobel, L. Kienle, E. Quandt, M. Wuttig, Ultralow-fatigue shape memory alloy films, Science 348(6238) (2015) 1004-1007.

[23] X. Huang, G.J. Ackland, K.M. Rabe, Crystal structures and shape-memory behaviour of NiTi, Nature materials 2(5) (2003) 307-311.

[24] K.G. Vishnu, A. Strachan, Phase stability and transformations in NiTi from density functional theory calculations, Acta Materialia 58(3) (2010) 745-752.

[25] M.-X. Wagner, W. Windl, Lattice stability, elastic constants and macroscopic moduli of NiTi martensites from first principles, Acta Materialia 56(20) (2008) 6232-6245.

[26] D. Holec, M. Friák, A. Dlouhý, J. Neugebauer, Ab initio study of pressure stabilized NiTi allotropes: Pressure-induced transformations and hysteresis loops, Physical Review B 84(22) (2011) 224119.

[27] S.R. Bakhtiari, J.Z. Liu, B.S. Shariat, H. Yang, Y. Liu, Role of hydrostatic pressure on the phase stability, the ground state, and the transformation pathways of NiTi alloy, Scripta Materialia 151 (2018) 57-60.

[28] W.-S. Ko, Temperature dependence of NiTi martensite structures: Density functional theory calculations, Scripta Materialia 154 (2018) 134-138.

[29] S. Kibey, H. Sehitoglu, D. Johnson, Energy landscape for martensitic phase transformation in shape memory NiTi, Acta Materialia 57(5) (2009) 1624-1629.

[30] T.H. Nam, T. Saburi, Y. Nakata, K.i. Shimizu, Shape memory characteristics and lattice deformation in Ti–Ni–Cu alloys, Materials Transactions, JIM 31(12) (1990) 1050-1056.

[31] W. Tang, R. Sandström, Z. Wei, S. Miyazaki, Experimental investigation and thermodynamic calculation of the Ti-Ni-Cu shape memory alloys, Metallurgical and materials transactions A 31(10) (2000) 2423-2430.

[32] P. Potapov, A. Shelyakov, D. Schryvers, On the crystal structure of TiNi-Cu martensite, Scripta materialia 44(1) (2001) 1-7.

[33] T. Ohba, T. Taniwaki, H. Miyamoto, K. Otsuka, K. Kato, In situ observations of martensitic transformations in Ti50Ni34Cu16 alloy by synchrotron radiation, Materials Science and Engineering: A 438 (2006) 480-484.

[34] T. Goryczka, M. Karolus, P. Ochin, H. Morawiec, Martensites in NiTi and NiTiCu alloys-Structure of melt spun Ni25Ti50Cu25 ribbons studied by X-ray diffraction, Journal de Physique-Colloques 11(8) (2001) 345-350.

[35] G. Kresse, D. Joubert, From ultrasoft pseudopotentials to the projector augmented-wave method, Physical Review B 59(3) (1999) 1758.

[36] J.P. Perdew, K. Burke, M. Ernzerhof, Generalized gradient approximation made simple, Physical review letters 77(18) (1996) 3865.

[37] P.E. Blöchl, Projector augmented-wave method, Physical review B 50(24) (1994) 17953.

[38] D. Sheppard, P. Xiao, W. Chemelewski, D.D. Johnson, G. Henkelman, A generalized solid-state nudged elastic band method, The Journal of chemical physics 136(7) (2012) 074103.

[39] A. Zunger, S.-H. Wei, L. Ferreira, J.E. Bernard, Special quasirandom structures, Physical Review Letters 65(3) (1990) 353.

[40] Y. Kudoh, M. Tokonami, S. Miyazaki, K. Otsuka, Crystal structure of the martensite in Ti-49.2 at.% Ni alloy analyzed by the single crystal X-ray diffraction method, Acta Metallurgica 33(11) (1985) 2049-2056.

[41] A. Togo, I. Tanaka, First principles phonon calculations in materials science, Scripta Materialia 108 (2015) 1-5.